Article

Progress in the Prediction of Entropy Generation in Turbulent Reacting Flows Using Large Eddy Simulation

Mehdi Safari [†]**, Fatemeh Hadi and M. Reza H. Sheikhi** *

Department of Mechanical and Industrial Engineering, Northeastern University, Boston, MA 02115, USA; E-Mails: safarim@miamioh.edu (M.S.); pourmohamadhadifar.f@husky.neu.edu (F.H.)

[†] Current Address: Department of Mechanical and Manufacturing Engineering, Miami University, Oxford, OH 45056, USA.

* Author to whom correspondence should be addressed; E-Mail: sheikhi@neu.edu; Tel.: +1-617-373-3427.

External Editor: Marc A. Rosen

Abstract: An overview is presented of the recent developments in the application of large eddy simulation (LES) for prediction and analysis of local entropy generation in turbulent reacting flows. A challenging issue in such LES is subgrid-scale (SGS) modeling of filtered entropy generation terms. An effective closure strategy, recently developed, is based on the filtered density function (FDF) methodology with inclusion of entropy variations. This methodology, titled entropy FDF (En-FDF), is the main focus of this article. The En-FDF has been introduced as the joint velocity-scalar-turbulent frequency-entropy FDF and the marginal scalar-entropy FDF. Both formulations contain the chemical reaction and its entropy generation effects in closed forms. The former constitutes the most comprehensive form of the En-FDF and provides closure for all of the unclosed terms in LES transport equations. The latter is the marginal En-FDF and accounts for entropy generation effects, as well as scalar-entropy statistics. The En-FDF methodologies are described, and some of their recent predictions of entropy statistics and entropy generation in turbulent shear flows are presented.

1. Introduction

Optimum use of energy is a major concern in designing modern energy conversion systems. According to the second law of thermodynamics, the energy efficiency in practice is always less than that expected theoretically, because of the irreversibilities in the system. Irreversibility essentially causes degradation of available energy into internal energy and, thus, destruction of the exergy (availability) of the working fluid [1]. This leads to a departure from thermodynamic ideality or reduction of the second-law efficiency. The rate of exergy destruction due to irreversibilities can be characterized in terms of entropy generation according to the Gouy–Stodola theorem, $I_D = T_a S_g$ [2,3], where I_D, T_a and S_g denote the rate of exergy destruction (also known as lost power), ambient (dead state) temperature and the entropy generation rate, respectively. Optimizing the energy efficiency thus relies on minimizing the overall exergy destruction, which can be achieved by minimizing the rate of entropy generated within the system [4–9].

During the past several decades, the second-law analysis has been the subject of broad investigations. These include system-level analysis, often termed exergy analysis, to obtain the net rate of exergy destruction [10–23]. More detailed studies involve identification of specific processes contributing to losses by considering the local generation of entropy. Such analysis has been performed on laminar flows in many studies. Teng *et al.* [24] derived the entropy transport equation to determine the rate of local entropy generation in multicomponent laminar reacting flows. Datta and Som [18] considered energy and exergy balance in a gas turbine combustor. Datta [25] conducted entropy generation analysis of a laminar diffusion flame. Nishida *et al.* [26] considered premixed and diffusion flames and identified important entropy generation and exergy loss mechanisms. Datta [27] studied the effect of gravity on the structure and generation of entropy in confined laminar diffusion flames. Shuja *et al.* [28] studied the influence of inlet velocity profile on the efficiency of heat transfer in a laminar jet. Briones *et al.* [29] studied the entropy generation processes in a partially-premixed flame. Sciacovelli and Verda [30] used an entropy generation minimization technique for design modifications in a tubular solid oxide fuel cell. Jiang *et al.* [31] presented an analysis of entropy generation in a hydrogen/air premixed micro-combustor with baffles, and Rana *et al.* [32] studied the exergy transfer and destruction due to premixed combustion in a heat recirculating micro-combustor.

In turbulent flows, there have been several studies involving direct numerical simulation (DNS). Okong'o and Bellan [33–35] performed comprehensive studies on entropy generation effects in supercritical, multicomponent shear flows; they suggested that, by containing the full extent of dissipative effects, entropy generation is useful to describe the behavior of small-scale turbulent motions. McEligot *et al.* [36] studied the entropy generation in the near wall region of a turbulent channel flow. Farran and Chakraborty [37] conducted DNS prediction of entropy generation in a turbulent premixed flame. Ghasemi *et al.* [38,39] used DNS and Reynolds averaged Navier–Stokes (RANS) to study the entropy generation and energy dissipation in transitional regions in wall shear flows. The prediction of entropy generation in the context of RANS has been carried out in many other studies. Stanciu *et al.* [40] performed the second-law analysis of a turbulent diffusion flame. Shuja *et al.* [41] studied local entropy generation in an impinging jet and used minimum entropy concept to evaluate various turbulence models. Adeyinka and Naterer [42] provided a model for the entropy transport equation in turbulent flows. Kock

and Herwig [43] provided wall functions for entropy production and performed analysis of entropy generation due to fluid flow and heat transfer in the near wall region of a pipe. Yapıcı *et al.* [44] performed local entropy generation in a methane-air burner. Herwig and Kock [45] used entropy generation as a tool for evaluating heat transfer performance in a turbulent shear flow. Stanciu *et al.* [46] studied the influence of swirl angle on the irreversibility in a turbulent diffusion flame, and Emadi and Emami [47] studied entropy generation in a turbulent hydrogen-enriched methane/air bluff-body flame. Despite the known advantages of large eddy simulation (LES) in turbulence modeling, the extent of its usage for entropy generation analysis has been insignificant. For the most part, this is due to the challenges in subgrid-scale (SGS) modeling of the unclosed irreversibility effects. An effective strategy for modeling of SGS effects is the filtered density function (FDF) methodology [48,49]. This methodology has been the subject of extensive previous contributions [50–62]. In recent works [63,64], a methodology based on filtered density function (FDF), termed the entropy FDF (En-FDF), has been introduced, which allows LES prediction of entropy transport and generation in turbulent reacting flows. This methodology has been presented as two formulations: the comprehensive and the marginal En-FDF. The comprehensive En-FDF contains the complete statistical information about the velocity, scalar, turbulent frequency and entropy fields and, thus, provides SGS closure for all of the unclosed moments in the filtered transport equations. The marginal En-FDF is the FDF of entropy and scalar fields and describes the unclosed entropy generation, chemical reaction and entropy-scalar statistics. This methodology is computationally more affordable and, thus, constitutes a more practical means of predicting entropy generation in complex turbulent reacting flows. However, it requires closure for all of the second order SGS moments via the conventional (non-FDF) LES models. The objective of this paper is to provide an overview of the state of progress in the application of En-FDF for LES prediction of entropy generation. Both En-FDF formulations are discussed along with their recent applications in LES of turbulent shear flows. Assessments of LES results against direct numerical simulation (DNS) and experimental data are also presented.

2. LES Formulation and Modeling

The primary transport variables in turbulent reacting flows, varying in space $\mathbf{x} \equiv x_i$ ($i = 1, 2, 3$) and time t, are the fluid density $\rho(\mathbf{x}, t)$, the velocity vector $\boldsymbol{u} \equiv u_i(\mathbf{x}, t)$ along the x_i direction, the specific enthalpy $h(\mathbf{x}, t)$, the specific entropy $s(\mathbf{x}, t)$, the pressure $p(\mathbf{x}, t)$ and the mass fractions of N_s species, $Y_\alpha(\mathbf{x}, t)$ ($\alpha = 1, 2, \ldots, N_s$), respectively. Implementation in LES involves the use of spatial filtering operation [65,66]: $\langle Q(\mathbf{x}, t) \rangle = \int_{-\infty}^{+\infty} Q(\mathbf{x}', t) G(\mathbf{x}', \mathbf{x}) \, d\mathbf{x}'$ where G denotes the filter function of width Δ and $\langle Q(\mathbf{x}, t) \rangle$ represents the filtered value of the transport variable $Q(\mathbf{x}, t)$. In reacting flows, it is convenient to consider the Favre filtered quantity, $\langle Q(\mathbf{x}, t) \rangle_L = \langle \rho Q \rangle / \langle \rho \rangle$. The transport variables satisfy the conservation equations of mass, momentum, energy and species mass fractions, as well as entropy transport equation. The filtered form of these equations are:

$$\frac{\partial \langle \rho \rangle}{\partial t} + \frac{\partial \langle \rho \rangle \langle u_i \rangle_L}{\partial x_i} = 0 \tag{1}$$

$$\frac{\partial \langle \rho \rangle \langle u_i \rangle_L}{\partial t} + \frac{\partial \langle \rho \rangle \langle u_i \rangle_L \langle u_j \rangle_L}{\partial x_j} = -\frac{\partial \langle p \rangle}{\partial x_i} + \frac{\partial \langle \tau_{ij} \rangle_L}{\partial x_j} - \frac{\partial \langle \rho \rangle \tau(u_i, u_j)}{\partial x_j} \tag{2}$$

$$\frac{\partial \langle \rho \rangle \langle \phi_\alpha \rangle_L}{\partial t} + \frac{\partial \langle \rho \rangle \langle u_i \rangle_L \langle \phi_\alpha \rangle_L}{\partial x_i} = \frac{\partial}{\partial x_i}\left(\gamma \frac{\partial \langle \phi_\alpha \rangle_L}{\partial x_i}\right) - \frac{\partial \langle \rho \rangle \tau(u_i, \phi_\alpha)}{\partial x_i} + \langle \rho S_\alpha \rangle \tag{3}$$

$$\frac{\partial \langle \rho \rangle \langle s \rangle_L}{\partial t} + \frac{\partial \langle \rho \rangle \langle u_i \rangle_L \langle s \rangle_L}{\partial x_i} = \frac{\partial}{\partial x_i}\left(\gamma \frac{\partial \langle s \rangle_L}{\partial x_i}\right) - \frac{\partial \langle \rho \rangle \tau(u_i, s)}{\partial x_i}$$
$$+ \left\langle \frac{1}{T}\tau_{ij}\frac{\partial u_i}{\partial x_j} \right\rangle + \left\langle \gamma \frac{c_p}{T^2}\frac{\partial T}{\partial x_i}\frac{\partial T}{\partial x_i} \right\rangle + \sum_{\alpha=1}^{N_s}\left\langle \frac{\gamma R_\alpha}{X_\alpha}\frac{\partial \phi_\alpha}{\partial x_i}\frac{\partial X_\alpha}{\partial x_i} \right\rangle - \left\langle \frac{\rho}{T}\sum_{\alpha=1}^{N_s}\mu_\alpha S_\alpha \right\rangle \tag{4}$$

where γ denotes the thermal and mass molecular diffusivity coefficients for all of the scalars. We assume unity Lewis number. In these equations, R_α, X_α and S_α are gas constant, mole fraction and chemical reaction source term for species α, respectively, and μ_α is the chemical potential per unit mass of species α. Variables T and c_p denote the temperature and the specific heat capacity at constant pressure for the mixture, respectively. We use the scalar array $\boldsymbol{\phi} = [\phi_1, \ldots, \phi_{N_s+1}]$ to represent mass fraction and enthalpy in a common form with $\phi_\alpha \equiv Y_\alpha$ for $\alpha = 1, \ldots, N_s$ and $\phi_{N_s+1} \equiv h$. We consider a Newtonian fluid and employ Fourier's law of heat conduction and Fick's law of mass diffusion. The viscous stress tensor τ_{ij} is thus represented as: $\tau_{ij} = \mu\left(\frac{\partial u_i}{\partial x_j} + \frac{\partial u_j}{\partial x_i} - \frac{2}{3}\frac{\partial u_k}{\partial x_k}\delta_{ij}\right)$ where μ is the fluid dynamic viscosity. In Equations (2)–(4), the second order SGS moments $\tau(a, b) = \langle ab \rangle_L - \langle a \rangle_L \langle b \rangle_L$ appear as unclosed. In addition, the filtered chemical reaction source term, the last term on the RHS of Equation (3), and the filtered entropy generation terms, the last four terms on the RHS of Equation (4), require SGS modeling. The modeled filtered entropy generation terms must be positive semidefinite according to the second law of thermodynamics. It is important to emphasize that filtered entropy and entropy generation cannot be obtained from other filtered variables, because of their nonlinear dependency. Moreover, it is clear that having entropy alone is not sufficient to account for the individual processes contributing to its generation.

The En-FDF provides an effective means of modeling the unclosed SGS effects. In its comprehensive form, the En-FDF, denoted by $\mathscr{F}_{en}\left(\hat{\boldsymbol{u}}, \hat{\boldsymbol{\phi}}, \hat{\omega}, \hat{s}, \mathbf{x}; t\right)$, contains complete statistical information about SGS variation of velocity, scalar, turbulent frequency $\omega(\mathbf{x}, t)$ and entropy fields. The En-FDF is defined as [63]:

$$\mathscr{F}_{en}\left(\hat{\boldsymbol{u}}, \hat{\boldsymbol{\phi}}, \hat{\omega}, \hat{s}, \mathbf{x}; t\right) = \int_{-\infty}^{+\infty} \rho(\mathbf{x}', t)\, \zeta\left[\hat{\boldsymbol{u}}, \hat{\boldsymbol{\phi}}, \hat{\omega}, \hat{s}\,; \boldsymbol{u}(\mathbf{x}', t), \boldsymbol{\phi}(\mathbf{x}', t), \omega(\mathbf{x}', t), s(\mathbf{x}', t)\right] G(\mathbf{x}' - \mathbf{x})d\mathbf{x}' \tag{5}$$

where:

$$\zeta\left[\hat{\boldsymbol{u}}, \hat{\boldsymbol{\phi}}, \hat{\omega}, \hat{s}\,; \boldsymbol{u}(\mathbf{x}, t), \boldsymbol{\phi}(\mathbf{x}, t), \omega(\mathbf{x}, t), s(\mathbf{x}, t)\right] = \delta\left(\hat{s} - s(\mathbf{x}, t)\right)\delta\left(\hat{\omega} - \omega(\mathbf{x}, t)\right) \times$$
$$\prod_{i=1}^{3}\delta\left(\hat{u}_i - u_i(\mathbf{x}, t)\right)\prod_{\alpha=1}^{N_s+1}\delta(\hat{\phi}_\alpha - \phi_\alpha(\mathbf{x}, t)) \tag{6}$$

is the fine-grained density [67] and δ denotes the Dirac delta function. In this formulation, the sample space variables $\hat{\boldsymbol{u}}, \hat{\boldsymbol{\phi}}, \hat{\omega}$ and $\hat{s}$ correspond to velocity vector, scalar array, turbulent frequency and entropy, respectively. The filtered value of any function $\tilde{Q}\left(\hat{\boldsymbol{u}}, \hat{\boldsymbol{\phi}}, \hat{\omega}, \hat{s}\right)$, fully defined by velocity, scalar, frequency and/or entropy, is obtained from the En-FDF as:

$$\langle \rho(\mathbf{x}, t) \rangle \langle Q(\mathbf{x}, t) \rangle_L = \iiiint_{-\infty}^{+\infty} \tilde{Q}\left(\hat{\boldsymbol{u}}, \hat{\boldsymbol{\phi}}, \hat{\omega}, \hat{s}\right) \mathscr{F}_{en}\left(\hat{\boldsymbol{u}}, \hat{\boldsymbol{\phi}}, \hat{\omega}, \hat{s}, \mathbf{x}; t\right) d\hat{\boldsymbol{u}}\, d\hat{\boldsymbol{\phi}}\, d\hat{\omega}\, d\hat{s} \tag{7}$$

The marginal En-FDF [64], denoted by $\mathscr{F}'_{en}\left(\hat{\boldsymbol{\phi}}, \hat{s}, \mathbf{x}; t\right)$, can be obtained from Equation (5) by integrating over $\hat{\boldsymbol{u}}$, $\hat{\omega}$ spaces. This form of En-FDF thus only contains information on joint scalar-entropy statistics. It is thus computationally more affordable for the prediction of complex turbulent reacting flows. Both forms of En-FDF are governed by exact transport equations, which include several unclosed terms [63,64]. The closure is provided by a stochastic model, which consists of a system of stochastic differential equations (SDEs). The stochastic model for the comprehensive form of En-FDF consists of SDEs for position, velocity, scalars, frequency and entropy:

$$dX_i^+ = U_i^+ dt + \sqrt{\frac{2\mu}{\langle\rho\rangle}}\,dW_i \tag{8a}$$

$$dU_i^+ = \left[-\frac{1}{\langle\rho\rangle}\frac{\partial\langle p\rangle}{\partial x_i} + \frac{1}{\langle\rho\rangle}\frac{\partial}{\partial x_j}\left(\mu\frac{\partial\langle u_i\rangle_L}{\partial x_j}\right) + \frac{1}{\langle\rho\rangle}\frac{\partial\langle\tau_{ij}\rangle_L}{\partial x_j} + G_{ij}\left(U_j^+ - \langle u_j\rangle_L\right)\right]dt$$
$$+ \sqrt{C_0\,k_s\,\Omega}\,dW_i' + \sqrt{\frac{2\mu}{\langle\rho\rangle}}\frac{\partial\langle u_i\rangle_L}{\partial x_j}\,dW_j \tag{8b}$$

$$d\phi_\alpha^+ = -C_\phi\,\Omega\,(\phi_\alpha^+ - \langle\phi_\alpha\rangle_L)\,dt + S_\alpha(\boldsymbol{\phi}^+)\,dt \tag{8c}$$

$$d\omega^+ = -C_\omega\,\Omega\left(\omega^+ - C_f\frac{k_s^{1/2}}{\Delta}\right)dt \tag{8d}$$

$$ds^+ = \frac{\epsilon_t}{T^+}\,dt + \frac{1}{T^+}\sum_{\alpha=1}^{N_s}\mu_\alpha^+ C_\phi\Omega(\phi_\alpha^+ - \langle\phi_\alpha\rangle_L)\,dt - \frac{1}{T^+}C_\phi\Omega(h^+ - \langle h\rangle_L)\,dt - \frac{1}{T^+}\sum_{\alpha=1}^{N_s}\mu_\alpha^+ S_\alpha(\boldsymbol{\phi}^+)\,dt \tag{8e}$$

where X_i^+, U_i^+, ω^+, ϕ_α^+, T^+, μ_α^+, h^+ and s^+ are the stochastic representations of position, velocity, frequency, scalars, temperature, chemical potential per unit mass of species α, specific enthalpy and specific entropy, respectively. The set of SDEs include the linear mean square estimation (LMSE) [67] and the simplified Langevin models [68], with $G_{ij} = -\Omega\left(\frac{1}{2} + \frac{3}{4}C_0\right)\delta_{ij}$. The W_i, W_i' terms denote the Wiener–Lévy processes [69]. In these equations, $k_s = \tau(u_i, u_i)/2$ denotes the SGS kinetic energy and Ω is the SGS mixing frequency, modeled as: $\Omega \equiv C_\Omega\langle\omega^+ | \omega^+ \geq \langle\omega\rangle_L\rangle_L$ [57]. The model parameters $C_0 = 2.1$, $C_\phi = 1$, $C_f = 1$, $C_\omega = 2$ and $C_\Omega = 0.9$ are set according to previous work [53,56,57]. The stochastic process corresponding to entropy (Equation (8e)) follows the Gibbs fundamental equation, in which ϵ_t is the total rate of turbulent dissipation, including both SGS and resolved contributions:

$$\epsilon_t = k_s\,\Omega + \frac{1}{\langle\rho\rangle}\left\langle\tau_{ij}\right\rangle\frac{\partial\langle u_i\rangle_L}{\partial x_j} \tag{9}$$

The Fokker–Planck equation [70] conjugate to the set of SDEs is the modeled transport equation for the comprehensive En-FDF:

$$\frac{\partial\mathscr{F}_{en}}{\partial t} + \frac{\partial(\hat{u}_i\,\mathscr{F}_{en})}{\partial x_i} = \frac{\partial}{\partial x_j}\left(\mu\frac{\partial(\mathscr{F}_{en}/\langle\rho\rangle)}{\partial x_j}\right) + \frac{1}{\langle\rho\rangle}\frac{\partial\langle p\rangle}{\partial x_i}\frac{\partial\mathscr{F}_{en}}{\partial\hat{u}_i} - \frac{1}{\langle\rho\rangle}\frac{\partial}{\partial x_j}\left(\mu\frac{\partial\langle u_i\rangle_L}{\partial x_j}\right)\frac{\partial\mathscr{F}_{en}}{\partial\hat{u}_i} - \frac{1}{\langle\rho\rangle}\frac{\partial\langle\tau_{ij}\rangle_L}{\partial x_j}\frac{\partial\mathscr{F}_{en}}{\partial\hat{u}_i}$$

$$-G_{ij}\frac{\partial}{\partial\hat{u}_i}\left[\left(\hat{u}_j - \langle u_j\rangle_L\right)\mathscr{F}_{en}\right] + \frac{\partial}{\partial x_j}\left(\frac{2\mu}{\langle\rho\rangle}\frac{\partial\langle u_i\rangle_L}{\partial x_j}\frac{\partial\mathscr{F}_{en}}{\partial\hat{u}_i}\right) + \frac{\mu}{\langle\rho\rangle}\frac{\partial\langle u_i\rangle_L}{\partial x_k}\frac{\partial\langle u_j\rangle_L}{\partial x_k}\frac{\partial^2\mathscr{F}_{en}}{\partial\hat{u}_i\partial\hat{u}_j} + \frac{1}{2}C_0\,k_s\,\Omega\frac{\partial^2\mathscr{F}_{en}}{\partial\hat{u}_i\partial\hat{u}_i}$$

$$+C_\phi\Omega\frac{\partial}{\partial\hat{\phi}_\alpha}\left[\left(\hat{\phi}_\alpha - \langle\phi_\alpha\rangle_L\right)\mathscr{F}_{en}\right] + C_\omega\Omega\frac{\partial}{\partial\hat{\omega}}\left[\left(\hat{\omega} - C_f\frac{k_s^{1/2}}{\Delta}\right)\mathscr{F}_{en}\right] - \frac{1}{T}\sum_{\alpha=1}^{N_s}C_\phi\Omega\left[\mu_\alpha\left(\hat{\phi}_\alpha - \langle\phi_\alpha\rangle_L\right)\right]\frac{\partial\mathscr{F}_{en}}{\partial\hat{s}}$$

$$-\frac{\epsilon_t}{T}\frac{\partial\mathscr{F}_{en}}{\partial\hat{s}} + \frac{1}{T}C_\phi\Omega\left(\hat{h} - \langle h\rangle_L\right)\frac{\partial\mathscr{F}_{en}}{\partial\hat{s}} - \sum_{\alpha=1}^{N_s}\frac{\partial}{\partial\hat{\phi}_\alpha}\left[S_\alpha(\hat{\boldsymbol{\phi}})\mathscr{F}_{en}\right] + \frac{1}{T}\sum_{\alpha=1}^{N_s}\mu_\alpha S_\alpha(\hat{\boldsymbol{\phi}})\frac{\partial\mathscr{F}_{en}}{\partial\hat{s}} \tag{10}$$

For the marginal En-FDF, the SDEs for the scalar and the entropy remain the same. However, the velocity and frequency must be obtained by other (non-FDF) means. In this case, the physical transport is modeled by [51]:

$$dX_i^+ = \left(\langle u_i \rangle_L + \frac{1}{\langle \rho \rangle} \frac{\partial (\gamma + \gamma_t)}{\partial x_i} \right) dt + \left(\sqrt{\frac{2(\gamma + \gamma_t)}{\langle \rho \rangle}} \right) dW_i \tag{11}$$

where the mixing frequency is modeled as $\Omega = (\gamma + \gamma_t)/\langle \rho \rangle \Delta^2$ [50,51] and γ_t denotes the SGS diffusivity. The Fokker–Planck equation corresponding to the set of SDEs (Equations (8c), (8e) and (11)) is the modeled transport equation for the marginal En-FDF:

$$
\begin{aligned}
\frac{\partial \mathscr{F}'_{en}}{\partial t} + \frac{\partial (\langle u_i \rangle_L \mathscr{F}'_{en})}{\partial x_i} &= \frac{\partial}{\partial x_j} \left((\gamma + \gamma_t) \frac{\partial (\mathscr{F}'_{en}/\langle \rho \rangle)}{\partial x_j} \right) + C_\phi \Omega \frac{\partial}{\partial \hat{\phi}_\alpha} \left[\left(\hat{\phi}_\alpha - \langle \phi_\alpha \rangle_L \right) \mathscr{F}'_{en} \right] \\
&- \frac{\epsilon_t}{T} \frac{\partial \mathscr{F}'_{en}}{\partial \hat{s}} - \frac{1}{T} \sum_{\alpha=1}^{N_s} C_\phi \Omega \left[\mu_\alpha \left(\hat{\phi}_\alpha - \langle \phi_\alpha \rangle_L \right) \right] \frac{\partial \mathscr{F}'_{en}}{\partial \hat{s}} + \frac{1}{T} C_\phi \Omega \left(\hat{h} - \langle h \rangle_L \right) \frac{\partial \mathscr{F}'_{en}}{\partial \hat{s}} \\
&- \sum_{\alpha=1}^{N_s} \frac{\partial}{\partial \hat{\phi}_\alpha} \left[S_\alpha(\hat{\boldsymbol{\phi}}) \mathscr{F}'_{en} \right] + \frac{1}{T} \sum_{\alpha=1}^{N_s} \mu_\alpha S_\alpha(\hat{\boldsymbol{\phi}}) \frac{\partial \mathscr{F}'_{en}}{\partial \hat{s}}
\end{aligned}
\tag{12}
$$

In both En-FDF formulations, the filtered chemical reaction and its entropy generation effect (the last two terms on the RHS of Equations (10) and (12)) appear in closed forms. Integrating Equation (10) according to Equation (7) yields the transport equations for all SGS moments implied by the En-FDF. The first entropy moment describes the transport of filtered entropy:

$$
\begin{aligned}
\frac{\partial \langle \rho \rangle \langle s \rangle_L}{\partial t} + \frac{\partial \langle \rho \rangle \langle u_i \rangle_L \langle s \rangle_L}{\partial x_i} &= \frac{\partial}{\partial x_i} \left(\gamma \frac{\partial \langle s \rangle_L}{\partial x_i} \right) - \frac{\partial \langle \rho \rangle \tau(u_i, s)}{\partial x_i} + \langle \rho \rangle \epsilon_t \left\langle \frac{1}{T} \right\rangle_L \\
&+ \langle \rho \rangle C_\phi \Omega \left[\sum_{\alpha=1}^{N_s} \tau \left(\phi_\alpha, \frac{g_\alpha}{T} \right) - \tau \left(h, \frac{1}{T} \right) \right] + \langle \rho \rangle C_\phi \Omega \sum_{\alpha=1}^{N_s} R_\alpha \tau (\phi_\alpha, \ln X_\alpha) - \left\langle \frac{\rho}{T} \sum_{\alpha=1}^{N_s} \mu_\alpha S_\alpha \right\rangle
\end{aligned}
\tag{13}
$$

where g_α is the Gibbs free energy per unit mass of species α. For the marginal En-FDF, a similar transport equation is obtained from Equation (12), but the SGS entropy flux is modeled as $\tau(u_i, s) = -\frac{\gamma_t}{\langle \rho \rangle} \frac{\partial \langle s \rangle_L}{\partial x_i}$. Comparing Equation (13) with Equation (4) reveals the En-FDF implied modeling of the individual filtered entropy generation terms:

$$
\begin{aligned}
\left\langle S_{gV} \right\rangle &= \left\langle \frac{1}{T} \tau_{ij} \frac{\partial u_i}{\partial x_j} \right\rangle \approx \langle \rho \rangle \left\langle \frac{1}{T} \right\rangle_L \epsilon_t \\
\left\langle S_{gH} \right\rangle &= \left\langle \gamma \frac{c_p}{T^2} \frac{\partial T}{\partial x_i} \frac{\partial T}{\partial x_i} \right\rangle \approx \langle \rho \rangle C_\phi \Omega \left[\sum_{\alpha=1}^{N_s} \tau \left(\phi_\alpha, \frac{g_\alpha}{T} \right) - \tau \left(h, \frac{1}{T} \right) \right] \\
\left\langle S_{gM} \right\rangle &= \left\langle \sum_{\alpha=1}^{N_s} \gamma R_\alpha \frac{1}{X_\alpha} \frac{\partial \phi_\alpha}{\partial x_i} \frac{\partial X_\alpha}{\partial x_i} \right\rangle \approx \langle \rho \rangle C_\phi \Omega \sum_{\alpha=1}^{N_s} R_\alpha \tau (\phi_\alpha, \ln X_\alpha)
\end{aligned}
\tag{14}
$$

It is noted that the filtered entropy generation by chemical reaction $\left\langle S_{gC} \right\rangle = -\left\langle \frac{\rho}{T} \sum_{\alpha=1}^{N_s} \mu_\alpha S_\alpha \right\rangle$ in Equation (13) does not require modeling in the En-FDF.

For numerical solution of the En-FDF, a procedure shown to be effective in FDF simulations is the hybrid Eulerian/Lagrangian Monte Carlo (MC) method [53,56,57,63,64]. The Eulerian solver is typically a grid-based finite-difference (FD) or finite volume method. The FD solver used in these

simulations is based on a fourth order compact parameter scheme [71]. The Lagrangian solver is based on the MC method to solve the set of SDEs. In this method, an ensemble of MC particles is used to represent the FDF. These particles carry information regarding the FDF variables: position, velocity, scalars, turbulent frequency and/or entropy. From the numerical standpoint, the use of the MC method is significantly easier than solving the modeled FDF transport equations (e.g., Equation (10) or (12)) directly, as shown in previous studies [50–53,56,57,63,64]. The filtered moments are constructed on the grid points by ensemble averaging the MC particles inside an ensemble domain around each grid point. The transfer of information from the grid points to MC particles is done by interpolation.

3. Simulations

In this section, we present some of the recent results pertaining to LES prediction of entropy statistics and entropy generation in turbulent shear flows. These include LES of a non-reacting temporal mixing layer and a turbulent jet flame. The former involves the comprehensive En-FDF formulation and gives assessment of this methodology against DNS data. The latter involves the marginal En-FDF and shows validation of En-FDF against laboratory data. These results demonstrate the capacity of LES/En-FDF in predicting entropy transport and generation in turbulent mixing and reacting flows.

The comprehensive form of En-FDF is applied for LES of a temporal mixing layer involving the transport of passive scalars. The objective is to assess the En-FDF prediction of entropy filtered moments and its rate of generation against DNS data. Large eddy simulation of this flow using various FDF methodologies are reported in [52,53,56,57,63]. In the following, we present some of the latest results obtained from the En-FDF. The variables are non-dimensionalized with the corresponding reference values: the reference length L_o is half of the initial vorticity thickness; the reference velocity U_o is half of the velocity difference across the shear layer; and the reference temperature is $T_o = 298\,K$. The Reynolds number based on these values is $Re_o = 50$. We assume unity Schmidt Sc and Prandtl Pr numbers. The computational domain spans $0 \leq x \leq L$, $\frac{-L}{2} \leq y \leq \frac{L}{2}$, $0 \leq z \leq L$ where $L = L_v/L_o$, and L_v is specified, such that $L_v = 2^{N_v}\lambda_u$, where N_v is the desired number of successive vortex pairings and λ_u is the wavelength of the most unstable mode corresponding to the mean streamwise velocity profile imposed at the initial time; x, y and z denote the streamwise, the cross-stream and the spanwise coordinate directions, respectively. The velocity components along these directions are denoted by u, v and w, respectively. The filtered normalized streamwise velocity, density and passive scalar (mixture fraction) ϕ fields are initialized using hyperbolic tangent profiles with free-stream conditions as: $\langle u \rangle_L = 1$, $\langle \rho \rangle = 0.5$ and $\langle \phi \rangle_L = 1$ on the top and $\langle u \rangle_L = -1$, $\langle \rho \rangle = 1$ and $\langle \phi \rangle_L = 0$ on the bottom. With the uniform initial pressure field, the initial filtered temperature is obtained from $\langle \rho \rangle$ according to the ideal-gas equation of state. To obtain the entropy generation by mass diffusion, we consider the top and bottom streams to carry H_2 and F_2, respectively. The flow involves pure mixing of these species; thus, mass fraction and enthalpy values are fully determined by the mixture fraction. The En-FDF predictions are assessed with DNS results. Simulations using LES and DNS are performed on 33^3 and 193^3 grid points, respectively. The LES filter size is twice as large as grid spacing in each direction. For comparison, the DNS data is filtered via a top-hat filter. The periodic boundary condition is used in the streamwise and spanwise directions, and

the zero-derivative boundary condition is employed at cross-stream boundaries. The initial number of particles per grid point is 320, and the ensemble domain size is set equal to half the grid spacing in each direction. Initialization of the MC particles and their treatment at the boundaries are consistent with the FD initial and boundary conditions.

Figure 1. Isosurfaces of instantaneous filtered entropy in temporal mixing layer simulations at $t = 80$, predicted by (**a**) entropy filtered density function (En-FDF) and (**b**) direct numerical simulation (DNS).
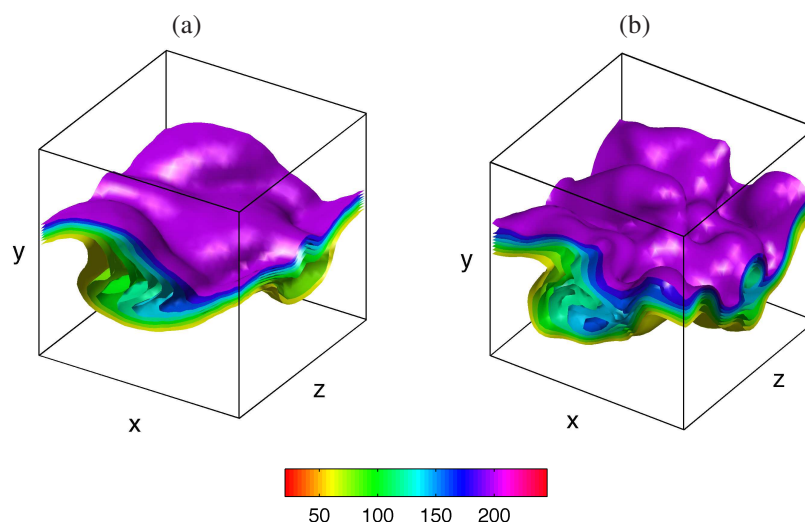
Figure 1 shows the formation of three-dimensional (3D) structures, visualized by the instantaneous filtered entropy fields obtained from the En-FDF and DNS. This figure shows a visual assessment of the methodology, as the large-scale coherent structures predicted by the En-FDF resemble those obtained from the DNS. Further appraisal is made by comparing the Reynolds-averaged statistics. These are constructed from the instantaneous data by spatial averaging over the homogeneous (streamwise and spanwise) directions and, hence, vary only in the cross-stream direction. The averaged quantities are denoted by an overbar. Figure 2 shows the close agreement of the Reynolds-averaged filtered entropy predicted by the En-FDF and DNS. To illustrate the En-FDF prediction of the second order SGS moments, the SGS, the resolved and the total entropy flux in the streamwise direction are shown in Figure 3. The resolved field is denoted by $\overline{R(u, s)}$, with $R(u, s) = \left(\langle u \rangle_L - \overline{\langle u \rangle_L}\right)\left(\langle s \rangle_L - \overline{\langle s \rangle_L}\right)$; the total field is $\overline{r(u, s)}$ with $r(u, s) = (u - \overline{u})(s - \overline{s})$. In DNS, the total component is directly available, while in LES, it is approximated by $\overline{r(u, s)} \approx \overline{R(u, s)} + \overline{\tau(u, s)}$ [72]. As shown, the streamwise entropy flux components are predicted well by the En-FDF. Similar agreements are obtained for other first and second order moments. The En-FDF is capable of accounting for individual filtered entropy generation effects. As shown in Figure 4, these are predicted favorably by the En-FDF. All mean entropy generation contributions peak in the fully turbulent region in the middle of the layer where the rate of turbulent mixing is the highest. The entropy generation by heat conduction is dominant in this flow, due to the large temperature difference across the layer, followed by that of mass diffusion. The effect of viscous dissipation is slightly underpredicted, due to underprediction of turbulent dissipation by the frequency model (Equation (8d)) [57]. However, the contribution of viscous dissipation to overall

entropy generation is much smaller than that of other effects. These simulations show the favorable agreement of En-FDF results with the DNS data.

Figure 2. Cross-stream variation of Reynolds-averaged filtered entropy obtained from temporal mixing layer simulations at $t = 80$. The solid line denotes the En-FDF prediction. The circles denote the filtered DNS data.
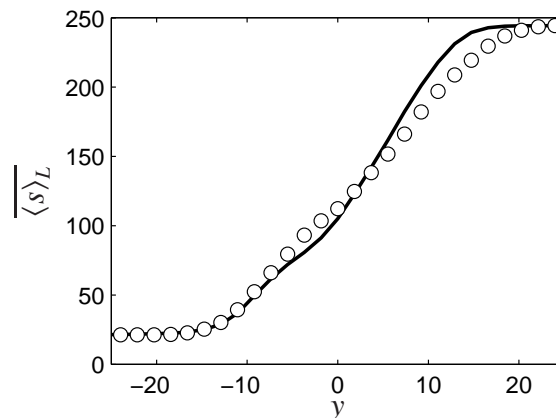
Figure 3. Cross-stream variation of Reynolds-averaged streamwise entropy flux components: (**a**) subgrid scale (SGS), (**b**) resolved and (**c**) total obtained from temporal mixing layer simulations at $t = 80$. The solid lines denote the En-FDF results, and the circles denote the filtered DNS data.
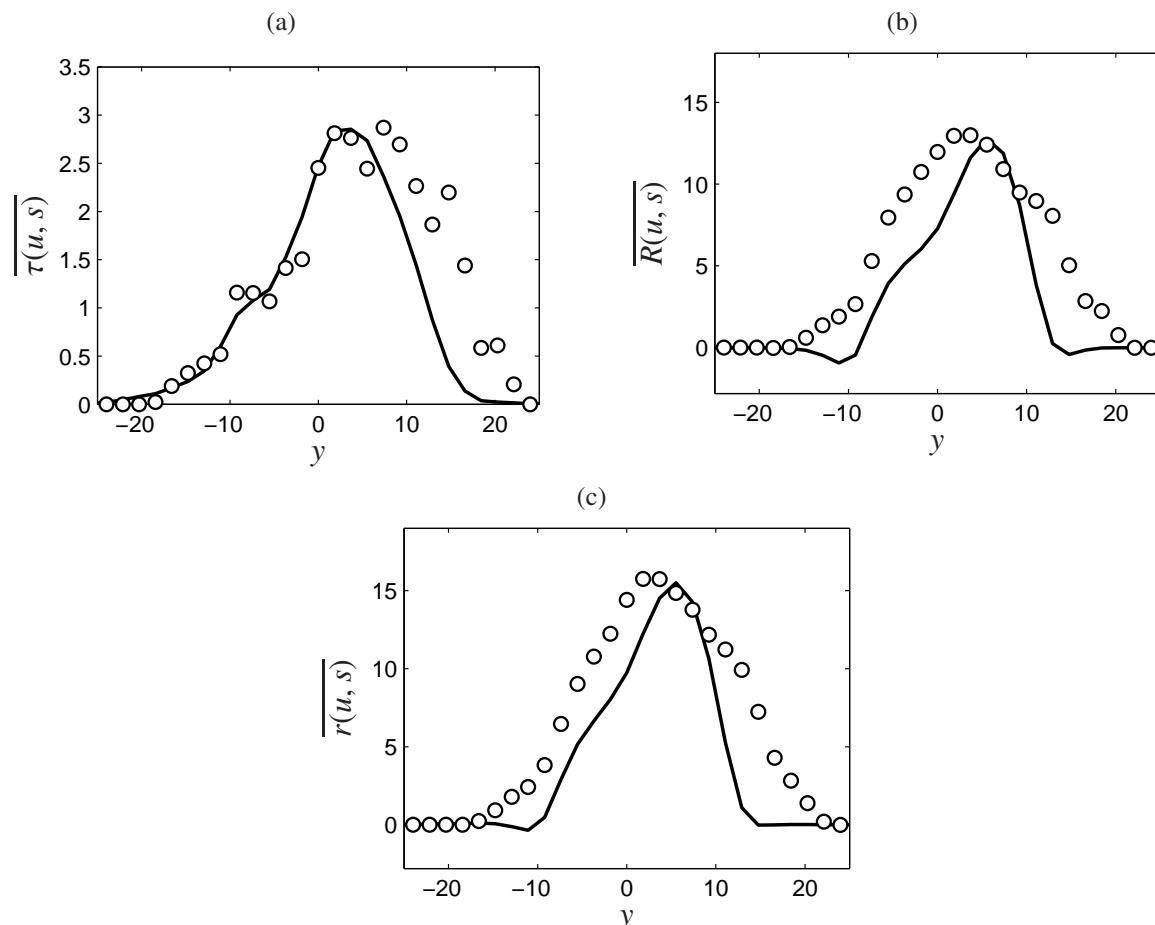
Figure 4. Cross-stream variation of Reynolds-averaged entropy generation effects: (**a**) total, (**b**) heat conduction, (**c**) mass diffusion and (**d**) viscous dissipation obtained from temporal mixing layer simulations at $t = 80$. The solid lines denote the En-FDF results, and the circles denote the filtered DNS data.
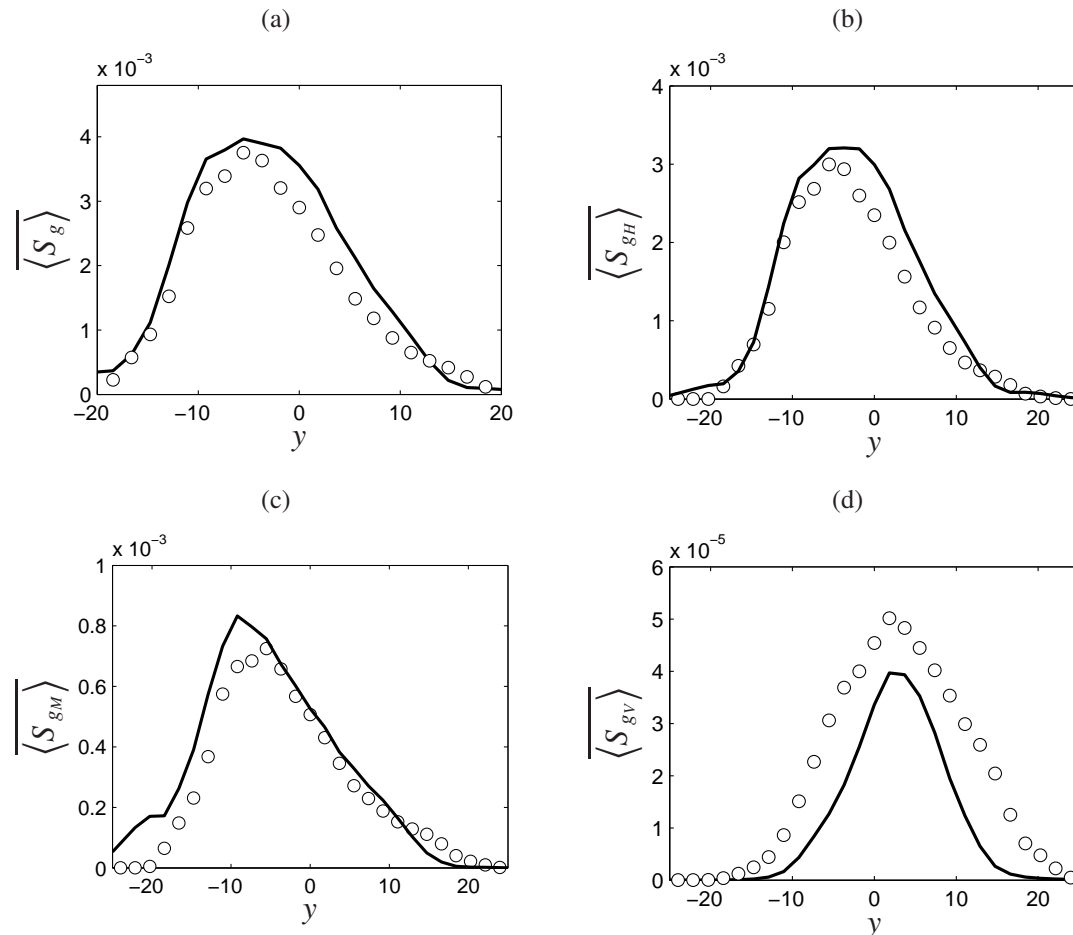
The marginal En-FDF formulation is applied for the LES of the turbulent non-premixed piloted methane jet flame (Sandia Flame D) [73,74]. The main objectives are to validate the En-FDF against laboratory data and to conduct entropy generation analysis of a realistic turbulent non-premixed flame. This flame has been the subject of several previous FDF studies [54,60,61,64]. Here, we discuss some of the latest results obtained via the En-FDF. The flame configuration includes a main jet with Reynolds number of $Re_D = 22,400$ based on the nozzle diameter $D = 7.2\,mm$ and the bulk jet velocity $U_b = 49.6\,m/s$. The coflow temperature is $T_c = 291\,K$. The flame is near equilibrium; thus, the methane oxidation kinetics is implemented using the flamelet concept [75], in which the detailed kinetics of Gas Research Institute [76] is employed in a laminar, one-dimensional counterflow (opposed jet) flame. The thermo-chemical variables are expressed as a function of the mixture fraction, which is carried as an additional passive scalar. The strain rate on the flame is assumed to be a constant value of $100\,s^{-1}$ [54]. The flow variables at the inflow are set similar to those in the experiment, including the inlet profiles of velocity and the mixture fraction. The molecular viscosity increases with $T^{0.7}$ and the molecular Schmidt (and Prandtl) number is $Sc = 0.75$. Simulations are conducted on a 3D Cartesian mesh with uniform grid spacings along all coordinate directions. The computational domain spans a region of $18D \times 10D \times 10D$ in the axial (x) and the two lateral (y, z) directions, respectively. The number of

grid points are $91 \times 101 \times 101$ in the x, y and z directions, respectively. The filter size is set equal to $\Delta = 2\sqrt[3]{\Delta x \Delta y \Delta z}$, where Δx, Δy and Δz denote grid spacing in the corresponding directions. The boundary conditions on FD domain boundaries are set according to the characteristic boundary conditions [77]. To account for all of the second order SGS moments in LES transport equations, the modified kinetic energy viscosity (MKEV) closure [51] is employed. The SGS modeling of the scalar and entropy fluxes is handled using $\gamma_t = \nu_t/Sc_t$, where the SGS viscosity ν_t is described by MKEV, and the turbulent Schmidt (and Prandtl) number is $Sc_t = 0.75$. The ensemble domain size is equal to the filter characteristic width, and there are approximately 48 MC particles participating in ensemble averaging at each grid point. According to extensive previous studies [50–53], this number of particles is sufficient to yield good statistical accuracy with minimal dispersion errors.

Figure 5 shows contours of the instantaneous filtered entropy obtained from the FD and MC solvers. The similarity of the instantaneous results indicates the consistency of the solvers in predicting the entropy field. In this figure, the fuel nozzle is located at the centerline of the $x = 0$ plane, surrounded by the pilot, which exhibits the highest temperature and entropy values. The region close to the nozzle is dominated by the molecular diffusion, and the flow resembles a laminar jet. Farther downstream, the growth of perturbations causes formation of large-scale coherent structures. The overall accuracy of the En-FDF predictions is assessed by comparing various statistics with the laboratory data; the experimental data for entropy statistics are constructed using the instantaneous data corresponding to the scalars. In the following, the notations $\overline{Q}$ and $RMS(Q)$ denote, respectively, the time-averaged mean and root mean square fields for a variable Q. To show the validation of En-FDF, some of the entropy statistics are presented here. In the following, the position, velocity, temperature and entropy are normalized by D, U_b, T_c and U_b^2/T_c, respectively. As shown in Figure 6, the radial ($r = \sqrt{z^2 + y^2}$) distributions of the time-averaged filtered entropy at $x = 7.5$ and $x = 15$ are in good agreement with the data. The validation of entropy RMS values is shown in Figure 7. The resolved RMS is $\overline{R(s,s)}^{1/2}$, where $R(s,s) = \left(\langle s \rangle_L - \overline{\langle s \rangle_L}\right)\left(\langle s \rangle_L - \overline{\langle s \rangle_L}\right)$, and the total RMS is $\overline{r(s,s)}^{1/2}$, where $r(s,s) \approx R(s,s) + \tau(s,s)$. The RMS values show reasonable agreements with the experimental data. The En-FDF prediction of the instantaneous, local entropy generation effects is illustrated in Figure 8. The entropy production by heat conduction shows local peaks in the inner (jet/pilot) shear layer near the nozzle and the fully turbulent regions downstream, where high temperature variations occur. Figure 8b depicts the entropy generation by mass diffusion in which local large values correspond with large gradients in species concentrations characterized by the mixture fraction. The contribution of the chemical reaction is shown in Figure 8c. As anticipated, this effect is dominant near the flame zone, identified by large temperature values. It is noted that experimental data for direct assessment of entropy generation predictions is not available for this flame; however, close agreement of filtered entropy with the data (Figure 6) indicates accurate prediction of entropy generation terms (Equation (4)). The mean entropy production at different axial locations (Figure 9) shows that near the nozzle, all irreversibilities exhibit peaks in the inner shear layer, due to large velocity and scalar gradients. At downstream locations, the heat conduction effect shows increased values caused by mixing of hot combustion products with the cold jet. A secondary peak due to this effect is also observed in the outer (pilot/coflow) shear layer at $x = 15$. For mass diffusion and chemical reaction, entropy generation profiles have similar shapes (Figure 9b,c), with peaks located near $r = 1$, where large concentration gradients occur because of chemical reaction. To

have a quantitative comparison of these effects, Figure 10 shows the entropy generation components along with the total entropy generation at two axial locations. Consistent with that discussed above, at $x = 5$, entropy generation effects are more localized in the inner shear layer region. The contribution of heat conduction is dominant, followed by chemical reaction and mass diffusion. As the turbulent jet develops downstream, all entropy production effects show larger spread in the radial direction, and the effect of chemical reaction becomes more significant. It is noticed that the effect of mass diffusion is less important, and that of viscous dissipation (not shown) is negligible in this flame. These simulations show the validation of LES/En-FDF against experimental data and the efficacy of this methodology in analysis of local entropy generation.
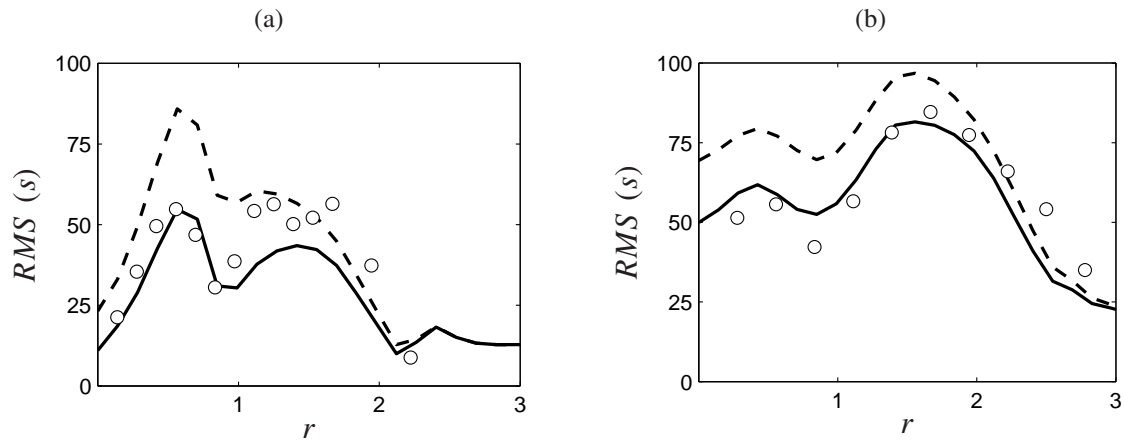
Figure 5. Instantaneous contours of filtered entropy in Sandia Flame D simulations obtained from the (**a**) Monte Carlo (MC) and (**b**) finite-difference (FD) solvers.
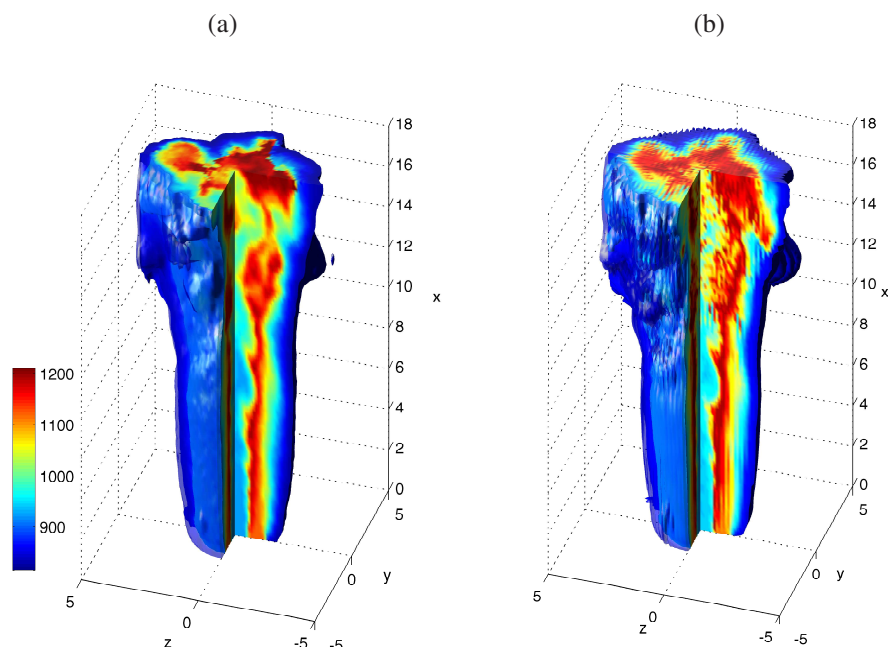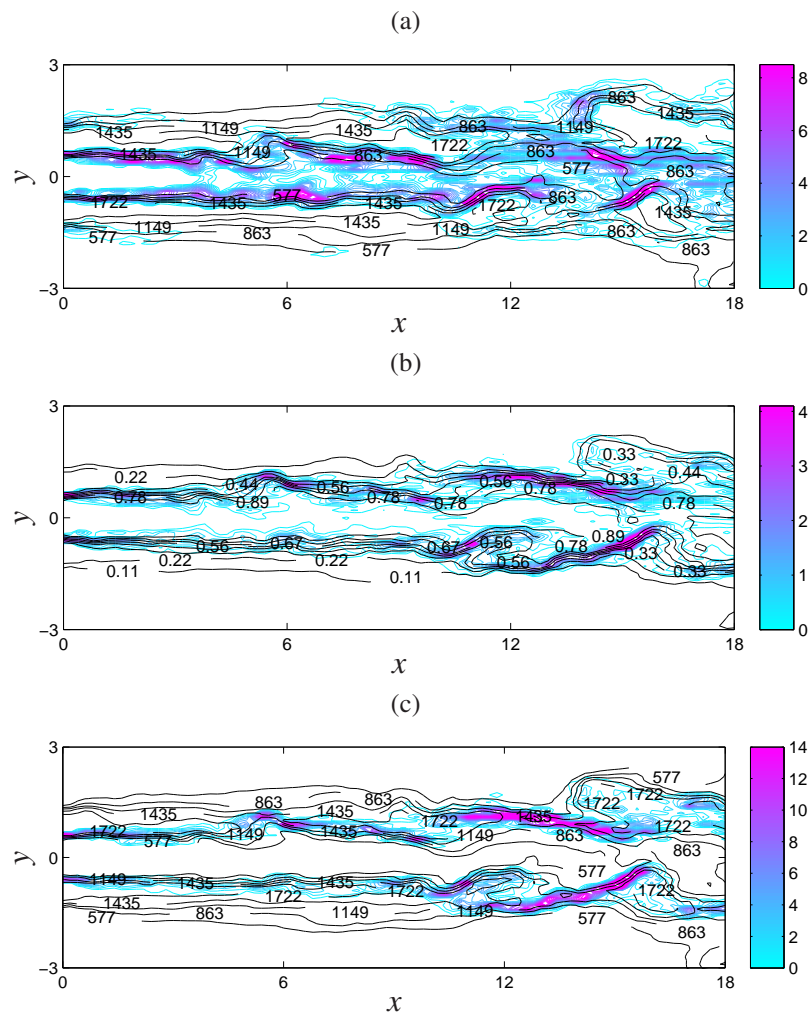

Figure 6. Radial variation of mean entropy in Sandia Flame D simulations at (**a**) $x = 7.5$ and (**b**) $x = 15$. The lines denote the En-FDF predictions. The circles denote the experimental data.
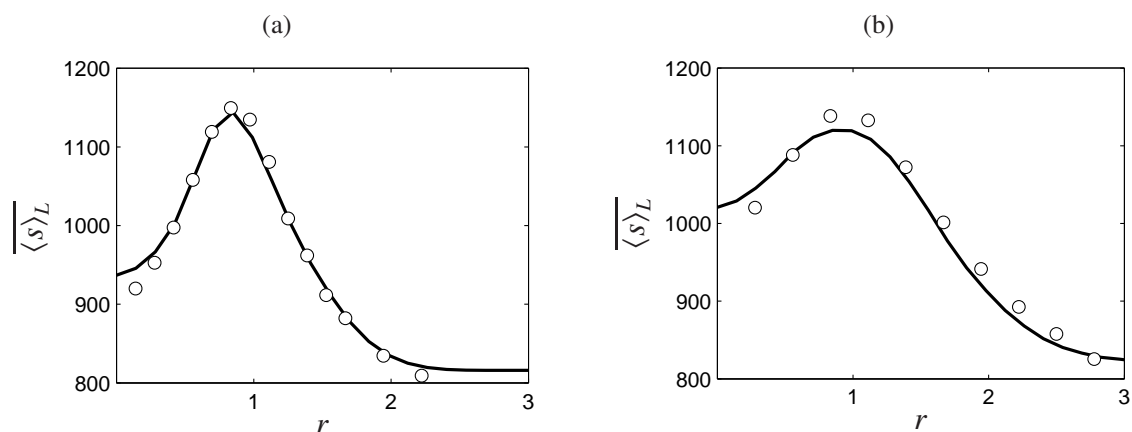
Figure 7. Radial variation of the RMS of entropy in Sandia Flame D simulations at (**a**) $x = 7.5$ and (**b**) $x = 15$. The solid and dashed lines denote the resolved and the total contributions, respectively. The circles denote the experimental data.


Figure 8. Instantaneous contours of entropy generation terms in Sandia Flame D simulations: (**a**) heat conduction (color) with temperature [K] (black) contours, (**b**) mass diffusion (color) with mixture fraction (black) contours and (**c**) chemical reaction (color) with temperature [K] (black) contours.

Figure 9. Radial variation of mean entropy generation rate due to (**a**) heat conduction, (**b**) mass diffusion and (**c**) chemical reaction in Sandia Flame D simulations at $x = 1$ ($\triangledown$), $x = 5$ ($\square$), $x = 10$ ($\lozenge$) and $x = 15$ ($-$).
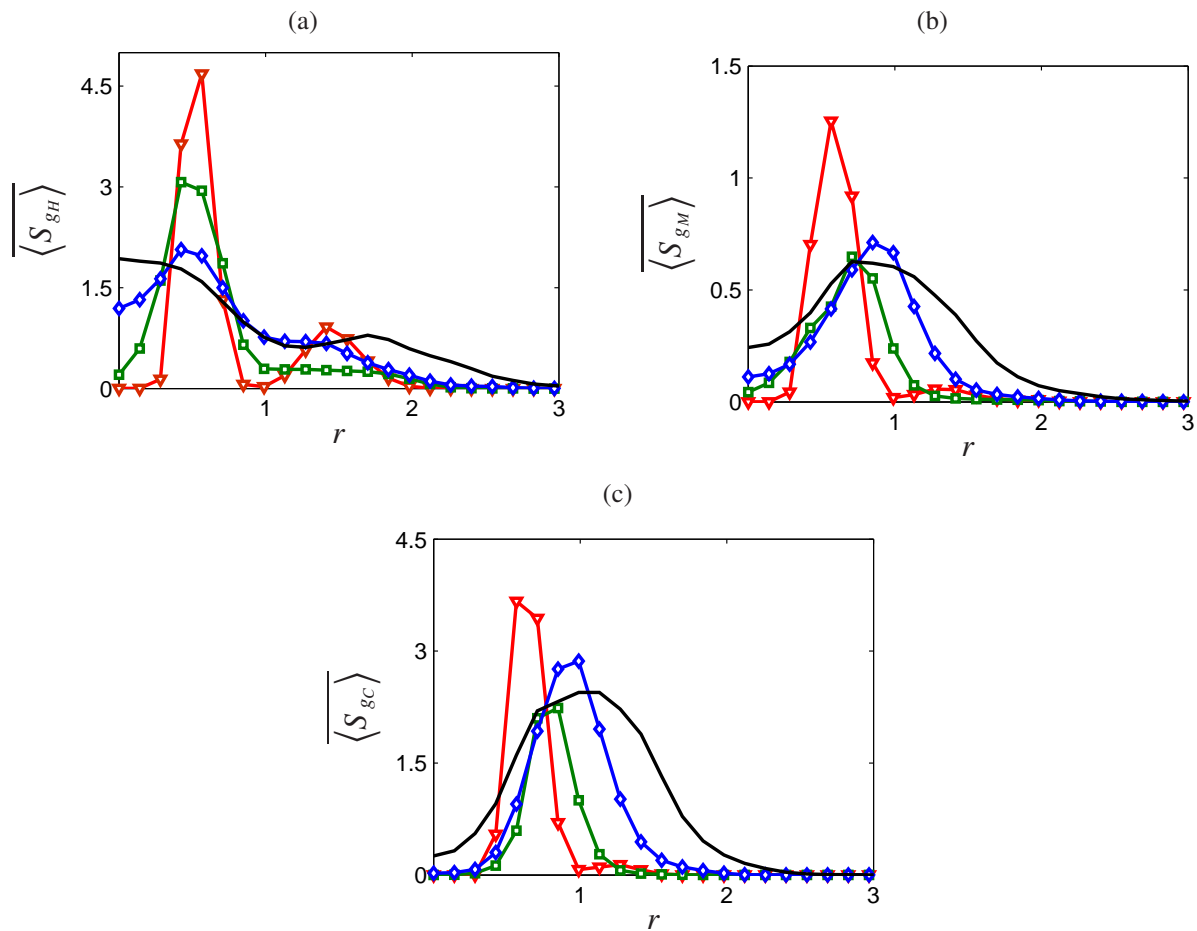
Figure 10. Radial variation of mean entropy generation rate (dashed lines) and its individual terms: heat conduction ($\triangledown$), mass diffusion ($\square$) and chemical reaction ($-$) at (**a**) $x = 5$ and (**b**) $x = 15$ in Sandia Flame D simulations.
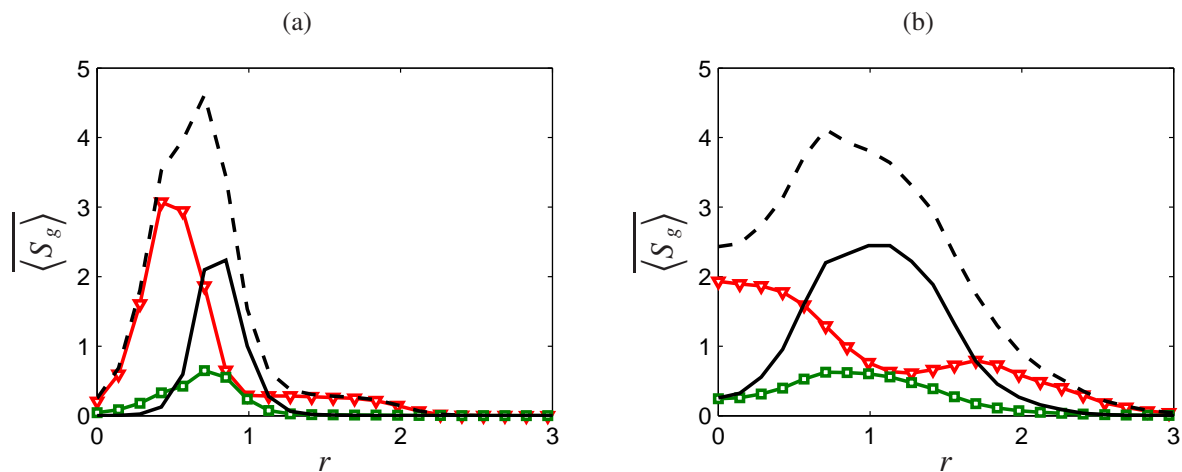
4. Final Remarks

Large eddy simulation (LES) is shown to be an effective approach to study local, transient entropy generation effects in turbulent mixing and reacting flows. Analysis of local entropy generation reveals the irreversible losses that contribute to the destruction of exergy and the reduction of second-law efficiency. An important issue in consideration of entropy transport equation in LES is subgrid-scale (SGS) modeling of the unclosed entropy generation effects corresponding to viscous dissipation, heat transfer, mass diffusion and chemical reaction. These SGS effects are described by the entropy filtered density function (En-FDF) methodology. The En-FDF is employed to simulate a turbulent shear layer and a turbulent non-premixed jet flame. The LES/En-FDF results show favorable agreements with direct numerical simulation (DNS) and experimental data. These simulations demonstrate the predictive capacity of the methodology and its effectiveness in the analysis of local entropy generation. In summary, some of the advantages provided by this approach are as follows: (1) the En-FDF accounts for all filtered moments of entropy in LES; (2) the En-FDF describes the individual entropy generation contributions, facilitating the second-law analysis of turbulent mixing and reacting flows; (3) in En-FDF, the chemical reaction and its entropy production effects appear in closed forms; (4) providing a unified description of dissipation, the entropy generation predicted by the En-FDF is beneficial to understand the behavior of small-scale motions in turbulent flows involving multi-physics phenomena; and (5) knowledge of entropy generation is also useful to study the effects of SGS closures and simulation parameters.

Author Contributions

All authors have contributed to the study and preparation of the article. They have read and approved the final manuscript.

Conflicts of Interest

The authors declare no conflict of interest.

References

1. Keenan, J.H. Availability and Irreversibility in Thermodynamics. *Br. J. Appl. Phys.* **1951**, *2*, 183–192.
2. Gouy, G. About Available Energy. *J. Phys. II* **1889**, *8*, 501–518.
3. Stodola, A. *Steam and Gas Turbines*; McGraw-Hill: New York, NY, USA, 1910.
4. Bejan, A. Fundamentals of Exergy Analysis, Entropy Generation Minimization, and the Generation of Flow Architecture. *Int. J. Energy Res.* **2002**, *26*, 545–565.

5. Bejan, A. Entropy Generation Minimization: The New Thermodynamics of Finite-Size Devices and Finite-Time Processes. *J. Appl. Phys.* **1996**, *79*, 1191–1218.

6. Mironova, V.A.; Tsirlin, A.M.; Kazakov, V.A.; Berry, R.S. Finite-Time Thermodynamics: Exergy and Optimization of Time-Constrained Processes. *J. Appl. Phys.* **1994**, *76*, 629–636.

7. Andresen, B. Current Trends in Finite-Time Thermodynamics. *Angew. Chem. Int. Ed.* **2011**, *50*, 2690–2704.

8. Som, S.K.; Datta, A. Thermodynamic Irreversibilities and Exergy Balance in Combustion Processes. *Prog. Energy Combust. Sci.* **2008**, *34*, 351–376.

9. Lior, N.; Sarmiento-Darkin, W.; Al-Sharqawi, H.S. The Exergy Fields in Transport Processes: Their Calculation and Use. *Energy* **2006**, *31*, 553–578.

10. Rakopoulos, C.D.; Michos, C.N. Generation of Combustion Irreversibilities in a Spark Ignition Engine Under Biogas-Hydrogen Mixtures Fueling. *Int. J. Hydrog. Energy* **2009**, *34*, 4422–4437.

11. Ugarte, S.; Metghalchi, M. Evolution of Adiabatic Availability and Its Depletion through Irreversible Processes. *Int. J. Exergy* **2005**, *2*, 109–119.

12. Klausner, J.F.; Li, Y.; Darwish, M.; Mei, R. Innovative Diffusion Driven Desalination Process. *J. Energy Resour. Technol.* **2004**, *126*, 219–225.

13. Narusawa, U. The Second-Law Analysis of Convective Pattern Change in a Rectangular Cavity. *J. Fluid Mech.* **1999**, *392*, 361–377.

14. Li, Z.W.; Chou, S.K.; Shu, C.; Yang, W.M. Entropy Generation During Microcombustion. *J. Appl. Phys.* **2005**, *97*, doi:10.1063/1.1876573.

15. Rezac, P.; Metghalchi, H. A Brief Note on the Historical Evolution and Present State of Exergy Analysis. *Int. J. Exergy* **2004**, *1*, 426–437.

16. Yilbas, B.S. Entropy Production During Laser Picosecond Heating of Copper. *J. Energy Resour. Technol.* **2002**, *124*, 204–213.

17. Gyftopoulos, E.P.; Beretta, G.P. Entropy Generation Rate In a Chemically Reacting System. *J. Energy Resour. Technol.* **1993**, *115*, 208–212.

18. Datta, A.; Som, S. Energy and Exergy Balance in a Gas Turbine Combustor. *Proc. Inst. Mech. Eng. Part A* **1999**, *213*, 23–32.

19. Hutchins, T.E.; Metghalchi, M. Energy and Exergy Analyses of the Pulse Detonation Engine. *J. Eng. Gas Turb. Power* **2003**, *125*, 1075–1080.

20. Jubeh, N.M. Exergy Analysis and Second Law Efficiency of a Regenerative Brayton Cycle with Isothermal Heat Addition. *Entropy* **2005**, *7*, 172–187.

21. Chavannavar, P.; Caton, J. Destruction of Availability (Exergy) Due to Combustion Processes: A Parametric Study. *Proc. Inst. Mech. Eng. Part A* **2006**, *220*, 655–668.

22. Sezer, I.; Altin, I.; Bilgin, A. Exergetic Analysis of Using Oxygenated Fuels in Spark-Ignition (SI) Engines. *Energy Fuels* **2009**, *23*, 1801–1807.

23. Chen, S.; Li, J.; Han, H.; Liu, Z.; Zheng, C. Effects of Hydrogen Addition on Entropy Generation in Ultra-Lean Counter-Flow Methane-Air Premixed Combustion. *Int. J. Hydrog. Energy* **2010**, *35*, 3891–3902.

24. Teng, H.; Kinoshita, C.M.; Masutani, S.M.; Zhou, J. Entropy Generation in Multicomponent Reacting Flows. *J. Energy Resour. Technol.* **1998**, *120*, 226–232.

25. Datta, A. Entropy Generation in a Confined Laminar Diffusion Flame. *Combust. Sci. Technol.* **2000**, *159*, 39–56.

26. Nishida, K.; Takagi, T.; Kinoshita, S. Analysis of Entropy Generation and Exergy Loss During Combustion. *Proc. Combust. Inst.* **2002**, *29*, 869–874.

27. Datta, A. Effects of Gravity on Structure and Entropy Generation of Confined Laminar Diffusion Flames. *Int. J. Therm. Sci.* **2005**, *44*, 429–440.

28. Shuja, S.Z.; Yilbas, B.S.; Khan, M. Entropy Generation in Laminar Jet: Effect of Velocity Profiles at Nozzle Exit. *Heat Mass Transf.* **2006**, *42*, 771–777.

29. Briones, A.M.; Mukhopadhyay, A.; Aggarwal, S.K. Analysis of Entropy Generation in Hydrogen-Enriched Methane-Air Propagating Triple Flames. *Int. J. Hydrog. Energy* **2009**, *34*, 1074–1083.

30. Sciacovelli, A.; Verda, V. Entropy Generation Minimization in a Tubular Solid Oxide Fuel Cell. *J. Energy Resour. Technol.* **2010**, *132*, doi:10.1115/1.4001063.

31. Jiang, D.; Yang, W.; Chua, K.J.; Ouyang, J.; Teng, J.H. Analysis of Entropy Generation Distribution in Micro-Combustors With Baffles. *Int. J. Hydrog. Energy* **2014**, *39*, 8118–8125.

32. Rana, U.; Chakraborty, S.; Som, S.K. Thermodynamics of Premixed Combustion in a Heat Recirculating Micro Combustor. *Energy* **2014**, *68*, 510–518.

33. Okong'o, N.; Bellan, J. Entropy Production of Emerging Turbulent Scales in a Temporal Supercritical n-Heptane/Nitrogen Three Dimensional Mixing Layer. *Proc. Combust. Inst.* **2000**, *28*, 467–504.

34. Okong'o, N.; Bellan, J. Direct Numerical Simulation of a Transitional Supercritical Binary Mixing Layer: Heptane and Nitrogen. *J. Fluid Mech.* **2002**, *464*, 1–34.

35. Okong'o, N.A.; Bellan, J. Small-Scale Dissipation in Binary-Species, Thermodynamically Supercritical, Transitional Mixing Layers. *Comput. Fluids* **2010**, *39*, 1112–1124.

36. McEligot, D.M.; Nolan, K.P.; Walsh, E.J.; Laurien, E. Effects of Pressure Gradients on Entropy Generation in the Viscous Layers of Turbulent Wall Flows. *Int. J. Heat Mass Transf.* **2008**, *51*, 1104–1114.

37. Farran, R.; Chakraborty, N. A Direct Numerical Simulation-Based Analysis of Entropy Generation in Turbulent Premixed Flames. *Entropy* **2013**, *15*, 1540–1566.

38. Ghasemi, E.; McEligot, D.M.; Nolan, K.P.; Crepeau, J.; Tokuhiro, A.; Budwig, R.S. Entropy Generation in a Transitional Boundary Layer Region Under the Influence of Freestream Turbulence Using Transitional RANS Models And DNS. *Int. Commun. Heat Mass Transf.* **2013**, *41*, 10–16.

39. Ghasemi, E.; McEligot, D.M.; Nolan, K.P.; Crepeau, J.; Siahpush, A.; Budwig, R.S.; Tokuhiro, A. Effects of Adverse and Favorable Pressure Gradients on Entropy Generation in a Transitional Boundary Layer Region Under the Influence of Freestream Turbulence. *Int. J. Heat Mass Transf.* **2014**, *77*, 475–488.

40. Stanciu, D.; Isvoranu, D.; Marinescu, M.; Gogus, Y. Second Law Analysis of Diffusion Flames. *Int. J. Appl. Thermodyn.* **2001**, *4*, 1–18.

41. Shuja, S.Z.; Yilbas, B.S.; Budair, M.O. Local Entropy Generation in an Impinging Jet: Minimum Entropy Concept Evaluating Various Turbulence Models. *Comput. Meth. Appl. Mech. Eng.* **2001**, *190*, 3623–3644.

42. Adeyinka, O.B.; Naterer, G.F. Modeling of Entropy Production in Turbulent Flows. *J. Fluids Eng.* **2004**, *126*, 893–899.

43. Kock, F.; Herwig, H. Local Entropy Production in Turbulent Shear Flows: A High-Reynolds Number Model with Wall Functions. *Int. J. Heat Mass Transf.* **2004**, *47*, 2205–2215.

44. Yapıcı, H.; Kayataş, N.; Albayrak, B.; Baştürk, G. Numerical Calculation of Local Entropy Generation in a Methane-Air Burner. *Energ. Convers. Manag.* **2005**, *46*, 1885–1919.

45. Herwig, H.; Kock, F. Local Entropy Production in Turbulent Shear Flows: A Tool For Evaluating Heat Transfer Performance. *J. Therm. Sci.* **2006**, *15*, 159–167.

46. Stanciu, D.; Marinescu, M.; Dobrovicescu, A. The Influence of Swirl Angle on the Irreversibilities in Turbulent Diffusion Flames. *Int. J. Thermodyn.* **2007**, *10*, 143–153.

47. Emadi, A.; Emami, M.D. Analysis of Entropy Generation in a Hydrogen-Enriched Turbulent Non-Premixed Flame. *Int. J. Hydrog. Energy* **2013**, *38*, 5961–5973.

48. Givi, P. Filtered Density Function for Subgrid Scale Modeling of Turbulent Combustion. *AIAA J.* **2006**, *44*, 16–23.

49. Ansari, N.; Jaberi, F.A.; Sheikhi, M.R.H.; Givi, P. Filtered Density Function as a Modern CFD Tool. In *Engineering Applications of CFD*; Maher, R.S., Ed.; Volume 1, Fluid Mechanics and Its Applications, Chapter 1; International Energy and Environment Foundation: Al-Najaf, Iraq, 2011; pp. 1–22.

50. Colucci, P.J.; Jaberi, F.A.; Givi, P.; Pope, S.B. Filtered Density Function for Large Eddy Simulation of Turbulent Reacting Flows. *Phys. Fluids* **1998**, *10*, 499–515.

51. Jaberi, F.A.; Colucci, P.J.; James, S.; Givi, P.; Pope, S.B. Filtered Mass Density Function for Large Eddy Simulation of Turbulent Reacting Flows. *J. Fluid Mech.* **1999**, *401*, 85–121.

52. Gicquel, L.Y.M.; Givi, P.; Jaberi, F.A.; Pope, S.B. Velocity Filtered Density Function for Large Eddy Simulation of Turbulent Flows. *Phys. Fluids* **2002**, *14*, 1196–1213.

53. Sheikhi, M.R.H.; Drozda, T.G.; Givi, P.; Pope, S.B. Velocity-Scalar Filtered Density Function for Large Eddy Simulation of Turbulent Flows. *Phys. Fluids* **2003**, *15*, 2321–2337.

54. Sheikhi, M.R.H.; Drozda, T.G.; Givi, P.; Jaberi, F.A.; Pope, S.B. Large Eddy Simulation of a Turbulent Nonpremixed Piloted Methane Jet Flame (Sandia Flame D). *Proc. Combust. Inst.* **2005**, *30*, 549–556.

55. Drozda, T.G.; Sheikhi, M.R.H.; Madnia, C.K.; Givi, P. Developments in Formulation and Application of the Filtered Density Function. *Flow Turbul. Combust.* **2007**, *78*, 35–67.

56. Sheikhi, M.R.H.; Givi, P.; Pope, S.B. Velocity-Scalar Filtered Mass Density Function for Large Eddy Simulation of Turbulent Reacting Flows. *Phys. Fluids* **2007**, *19*, doi:10.1063/1.2768953.

57. Sheikhi, M.R.H.; Givi, P.; Pope, S.B. Frequency-Velocity-Scalar Filtered Mass Density Function for Large Eddy Simulation of Turbulent Flows. *Phys. Fluids* **2009**, *21*, doi:10.1063/1.3153907.

58. Yaldizli, M.; Mehravaran, K.; Jaberi, F.A. Large-Eddy Simulations of Turbulent Methane Jet Flames with Filtered Mass Density Function. *Int. J. Heat Mass Transf.* **2010**, *53*, 2551–2562.

59. Yilmaz, S.L.; Nik, M.B.; Sheikhi, M.R.H.; Strakey, P.A.; Givi, P. An Irregularly Portioned Lagrangian Monte Carlo Method for Turbulent Flow Simulation. *J. Sci. Comput.* **2011**, *47*, 109–125.

60. Nik, M.; Yilmaz, S.; Sheikhi, M.R.H.; Givi, P. Grid Resolution Effects on VSFMDF/LES. *Flow Turbul. Combust.* **2010**, *85*, 677–688.

61. Nik, M.B.; Yilmaz, S.L.; Givi, P.; Sheikhi, M.R.H.; Pope, S.B. Simulation of Sandia Flame D Using Velocity-Scalar Filtered Density Function. *AIAA J.* **2010**, *48*, 1513–1522.

62. Ansari, N.; Pisciuneri, P.H.; Strakey, P.A.; Givi, P. Scalar-Filtered Mass-Density-Function Simulation of Swirling Reacting Flows on Unstructured Grids. *AIAA J.* **2012**, *50*, 2476–2482.

63. Sheikhi, M.R.H.; Safari, M.; Metghalchi, H. Large Eddy Simulation for Local Entropy Generation Analysis of Turbulent Flows. *J. Energy Resour. Technol.* **2012**, *134*, doi:10.1115/1.4007482.

64. Safari, M.; Sheikhi, M.R.H. Large Eddy Simulation for Prediction of Entropy Generation in a Nonpremixed Turbulent Jet Flame. *J. Energy Resour. Technol.* **2014**, *136*, doi:10.1115/1.4025974.

65. Sagaut, P. *Large Eddy Simulation for Incompressible Flows*; Springer-Verlag: New York, NY, USA, 2005.

66. Geurts, B.J. *Elements of Direct and Large-Eddy Simulation*; R.T. Edwards, Inc.: Philadelphia, PA, USA, 2004.

67. Pope, S.B. *Turbulent Flows*; Cambridge University Press: Cambridge, UK, 2000.

68. Haworth, D.C.; Pope, S.B. A Generalized Langevin Model for Turbulent Flows. *Phys. Fluids* **1986**, *29*, 387–405.

69. Gikhman, I.I.; Skorokhod, A.V. *Stochastic Differential Equations*; Springer-Verlag: New York, NY, USA, 1972.

70. Risken, H. *The Fokker-Planck Equation, Methods of Solution and Applications*; Springer-Verlag: New York, NY, USA, 1989.

71. Kennedy, C.A.; Carpenter, M.H. Several New Numerical Methods for Compressible Shear-Layer Simulations. *Appl. Numer. Math.* **1994**, *14*, 397–433.

72. Vreman, B.; Geurts, B.; Kuerten, H. Large-Eddy Simulation of the Turbulent Mixing Layer. *J. Fluid Mech.* **1997**, *339*, 357–390.

73. Barlow, R.S. Sandia National Laboratories, TNF Workshop website. Available online: http://www.ca.sandia.gov/TNF/abstract.html (accessed on 23 September 2014).

74. Frank, J.H.; Barlow, R.S. Simultaneous Rayleigh, Raman, and LIF Measurements in Turbulent Premixed Methane-Air Flames. *Proc. Combust. Inst.* **1998**, *27*, 759–766.

75. Peters, N. *Turbulent Combustion*; Cambridge University Press: Cambridge, UK, 2000.

76. GRI-Mech Home Page. Available online: http://www.me.berkeley.edu/gri_mech (accessed on 18 September 2014).

77. Poinsot, T.J.; Lele, S.K. Boundary Conditions for Direct Simulations of Compressible Viscous Flows. *J. Comput. Phys.* **1992**, *101*, 104–129.